# Backward-Wave Suppression Analysis, and Design and Fabrication of a Prototype Millimeter-Wave Ring-Bar Slow-Wave Structure

Sean Sengele, *Member, IEEE*, Marc L. Barsanti, Thomas A. Hargreaves, *Member, IEEE*, Carter M. Armstrong, *Fellow, IEEE*, John H. Booske, *Fellow, IEEE*, and Yue-Ying Lau, *Fellow, IEEE*

***Abstract*— A challenge for high-power millimeter-wave (mmw) traveling-wave tube (TWT) amplifiers is to realize high-power operation without incurring oscillation from backward-wave (BW) interaction. Conventional wisdom purports that contrawound (including ring bar) helix TWTs are superior to monofilar helix TWTs for stability against BW oscillations due to a zero or at least greatly suppressed BW interaction impedance ($K_{BW}$) compared with the forward-wave (FW) interaction impedance ($K_{FW}$). We use 3-D electromagnetic (EM) field calculations of a ring-bar helix to compare the BW and FW interaction impedances. Using a sine/cosine basis set and a comparison at a fixed phase velocity (rather than fixed frequency assumed in previous analyses), we show that the BW interaction impedance is not always significantly suppressed in the ring-bar/contrawound helix. In spite of the lack of ubiquitous BW stability, we use EM simulations to illustrate that there remain specific, efficient, high-gain mmw ring-bar designs with $K_{BW} < K_{FW}$. The accuracy of the simulations is validated by experimental measurements that confirm simulation predictions of phase velocity and S-parameters.**

***Index Terms*— Backward-wave (BW) mode, millimeter-wave (mmw), ring bar, traveling-wave tube (TWT).**

## I. Introduction

THE contrawound and ring-bar slow-wave structures (SWSs) have long been identified as viable alternatives to the helix SWS in both high-power and high-frequency traveling-wave tubes (TWTs) [1]–[4]. Traditionally, the contrawound and ring-bar SWSs have been promoted over the helix for these applications because they are claimed to provide:

1) a larger diameter at a given operating frequency;
2) an increased fundamental forward-wave (FW) mode interaction impedance;
3) a decreased backward-wave (BW) mode interaction impedance.

The larger circuit diameter allows for a larger, more powerful electron beam to propagate within the interior of the SWS. This, in combination with the increased fundamental FW mode interaction impedance, allows more beam power to be converted to the fundamental FW component of the electromagnetic (EM) wave in the TWT. This results in greater output power. Simultaneously, decreased BW interaction impedance results in a decrease in the amount of power being coupled to the BW mode, thereby decreasing the chance of unwanted oscillation in the TWT.

Contrawound and ring-bar SWSs also come with disadvantages. The most notable being that they provide a much narrower instantaneous 1-dB gain bandwidth compared with the helix SWS since they are significantly more dispersive [2]. In addition, unlike the ubiquitous helix SWS, these SWSs are used infrequently and therefore are often overlooked simply due to the unfamiliarity of their design fundamentals.

The contrawound and ring-bar SWSs have been explored theoretically using analytic and experimental techniques [1], [2], [5]–[7]. Although studies using these methods have been insightful, modern computational techniques, such as the finite-element method (FEM), offer the ability to look closer at the fields of an EM wave traveling along these SWSs. A deeper understanding of why these SWSs have both the advantages and disadvantages discussed above is gained by examining these EM field distributions. In addition, FEM models, such as those solved using Ansys' high-frequency structure simulator (HFSS) [8], allow for a parametric comparison that was previously unexplored using analytic theory. To best of our knowledge, there is only one published research effort on the computational simulation of a ring-bar SWS [9]. That analysis, however, was limited to the fundamental FW mode.

A principal finding in this paper is that the ring-bar's BW interaction impedance, $K_{BW}$, is not always much less than the FW impedance, $K_{FW}$, an assumption underlying the conventional wisdom that the contrawound SWS TWT is immune

Manuscript received June 19, 2014; revised October 10, 2014; accepted October 12, 2014. Date of publication November 20, 2014; date of current version December 9, 2014. This work was supported by the Electron Devices Division, L-3 Communications, San Carlos, CA, USA.

S. Sengele is with the Sensors and Electromagnetic Applications Laboratory, Georgia Tech Research Institute, Smyrna, GA 30080 USA (e-mail: sean.sengele@gtri.gatech.edu).

M. L. Barsanti, T. A. Hargreaves, and C. M. Armstrong are with the Electron Devices Division, L-3 Communications, San Carlos, CA 94070 USA (e-mail: marc.barsanti@l-3com.com; tom.hargreaves@l-3com.com; carter.armstrong@l-3com.com).

J. H. Booske is with the Department of Electrical and Computer Engineering, University of Wisconsin-Madison, Madison, WI 53706 USA (e-mail: booske@engr.wisc.edu).

Y.-Y. Lau is with the Department of Nuclear Engineering and Radiological Sciences, University of Michigan, Ann Arbor, MI 48109 USA (e-mail: yylau@umich.edu).

Color versions of one or more of the figures in this paper are available online at http://ieeexplore.ieee.org.

Digital Object Identifier 10.1109/TPS.2014.2366243

from BW oscillation. The ratio of $K_{\mathrm{BW}}/K_{\mathrm{FW}}$ varies with SWS design and depends on which parameters are held fixed when making the comparison. Nevertheless, it still remains that specific designs can achieve a strong FW interaction and a weak BW interaction that includes $K_{\mathrm{BW}}/K_{\mathrm{FW}} < 1$, while realizing other advantageous features of contrawound SWS TWTs, such as high gain, high intrinsic efficiency, and/or high power. In Sections II and III, we examine the BW interaction. We start in Section II with deriving the calculation of the BW interaction impedance and examine how the BW fields are distributed within the SWS. In Section III, we compare the BW interaction impedance to the fundamental FW mode impedance and contrast it to the conventional viewpoint. In Section IV, we illustrate the fact that specific ring-bar SWS designs can still provide performance consistent with conventional expectations of high gain, high efficiency, and/or high power with a BW interaction that is significantly less than the fundamental FW interaction. The illustration case is a ring-bar SWS for a high-power millimeter-wave (mmw) ($Q$-band) TWT. Since the accuracy of this illustration hinges on the accuracy of HFSS computations, we fabricated several ring-bar SWSs and a cold-test structure and obtained experimental data on measurable properties, such as phase velocity and reflection and transmission S-parameters. The details of the experimental methods and measurements are provided in Section V and discussed in Section VI. The data agreed well with the HFSS predictions within reasonable tolerances, validating the accuracy of the computational model predictions. Finally, the conclusions are drawn in Section VII.

## II. Calculation of Backward-Wave Interaction Impedance for the Ring-Bar Slow-Wave Structure

The proficiency of an SWS to couple energy between the electron beam and the EM field can be quantified by a parameter called the interaction impedance, or Pierce impedance [10], [11]. Originally formulated in [12], the interaction impedance, $K$, is a measure of the energy stored in the axially directed electric field of the EM wave normalized to the EM power flowing along the SWS axis. It has units of ohms. In a coordinate system with the $z$-axis positioned in the center of the SWS, interaction impedance at a particular radius is defined as

$$K_{m,n}(\omega, \vec{r}) = \frac{|E_{z_{m,n}}(\omega, \vec{r})|^2}{2\beta^2(\omega) P_z(\omega)} \tag{1}$$

where $E_{z_{m,n}}$ is the Fourier amplitude of the axially directed electric field of the, $m$, azimuthal harmonic and the, $n$, spatial harmonic mode. This electric field is a function of both frequency, $\omega$, and position, $\vec{r}$. The parameter, $\beta = 2\pi/\lambda$, is the axial wavenumber of the EM wave where $\lambda$ is the frequency-dependent wavelength in the SWS, and $P_z$ is the time-averaged EM power flowing along the SWS, which can be calculated using the Poynting vector

$$P_z = \frac{1}{2}\mathrm{Re}\left\{\iint [\vec{E} \times \vec{H}^{\star}] \cdot d\vec{A}\right\} \tag{2}$$

where $\vec{E}$ and $\vec{H}^{\star}$ are the electric field and complex conjugate of the magnetic intensity, respectively, and the integration takes place over the cross-sectional area, $A$, through which the EM wave propagates.

For any spatially periodic structure, such as the helix or contrawound SWS, the total EM wave propagating along the SWS can be described as a sum of spatial harmonics that all have the same frequency but different propagation vectors [13]. In the case of the helix or contrawound SWS, the fundamental or FW mode is the lowest order mode and represents a wave with a phase and group velocity in the $+z$-direction. The BW mode is a separate mode and represents a wave with an effective phase velocity in the $+z$-direction but a group velocity in the $-z$-direction. Since there is an effective phase velocity in the $+z$-direction, the BW mode can still exchange energy with the traveling electron beam (also traveling in the $+z$-direction) even though its energy flow is in the opposite direction. The coupling of energy to the BW mode is a primary cause of unwanted oscillations in a TWT that is designed to be an amplifier.

The amount of energy coupled to the unwanted BW mode is quantified by calculating the interaction impedance. Frequently, the interaction impedance of the fundamental, FW mode is calculated solely along the axis of the SWS. Other choices have included at the drift-tube radius (e.g., for klystrons) or averaged over the expected beam's cross-sectional area. The advantage of the first two choices is that they characterize the strength of the beam-wave interaction without requiring time- and resource-intensive averages over 2-D or 3-D EM field distributions. The disadvantage of the on-axis impedance is that it will give a misleading value of zero for modes in which the axial electric field component vanishes on-axis but is nonzero off-axis. The drift-tube radius impedance is useful for klystrons but is not a particularly meaningful choice for TWTs. In this paper, we were particularly interested in the strength of the beam-wave interaction with the BW mode and comparing it with the beam-wave interaction strength of the fundamental FW mode. However, the electric field of the BW mode has a radial dependence that is roughly proportional to the first-order modified Bessel function of the first kind, $I_1$, which is zero on-axis. This is an example of a mode for which an off-axis or beam-averaged interaction impedance is a more appropriate indicator of the beam-wave interaction strength.

To investigate the basic conventional understanding that the ring-bar SWS, as an example of the contrawound SWS, is robustly stable against BW oscillation, we chose to examine and compare the BW mode's interaction impedance to the FW mode's impedance at a typical beam radius, which we took to be half the radius of the SWS. This comparison choice, rather than the full beam-averaged impedance comparison allowed us to qualitatively yet meaningfully reexamine previous conclusions on BW stability of contrawound SWSs (which were also based on a single-radius-on-axis-impedance analysis) without incurring extreme computational resource and time costs required for a full beam-averaged impedance comparison. As discussed in the following sections, the axial electric field distributions of the ring-bar modes are complicated, not amenable to analytic solution, not azimuthally

symmetric, and therefore require tedious full azimuthal as well as radial- and axial-period integrations of 3-D numerical computation data to obtain beam-averaged impedances.

### *A. Calculation of Off-Axis Interaction Impedance for Any Mode in a Helix Slow-Wave Structure*

For a periodic SWS, the total propagating EM wave can be described as a sum of spatial harmonics [13]. A unique set of mode numbers are used to denote each mode. For a conventional helix SWS, two numbers are necessary for mode identification. The azimuthal harmonic number, $m$, provides the number of $2\pi$ variations in the electric field's phase that occur azimuthally around a cross-sectional plane and the spatial harmonic number, $n$, provides the number of $2\pi$ advances of the electric field phase along one pitch of the SWS. Conventionally, we define the total axial electric field, $E_z(r, \theta, z)$, propagating along a helical SWS as a Fourier series given as

$$E_z(r, \theta, z) = \sum_m \sum_n E_{z_{m,n}}(r) e^{j(m\theta - \beta_n z)}. \tag{3}$$

As discussed in [14], if the electric field is known in all space for all modes in a helix, the Fourier coefficient, $E_{z_{m,n}}$, and the corresponding wavenumber, $\beta_n$, can be expressed as

$$E_{z_{m,n}}(r) = \frac{1}{2\pi p} \int_0^{2\pi} d\theta \int_0^{p} dz \cdot E_z(r, \theta, z) \cdot e^{j(\beta_n z - m\theta)} \tag{4}$$

$$\beta_n = \frac{\Delta\phi + 2\pi n}{p} \tag{5}$$

where $\Delta\phi$ is the phase advance in a single period of the SWS with pitch, $p$. The determination of $E_z(r, \theta, z)$ can be done analytically or using a computer code such as HFSS. The Pierce interaction impedance for a single space harmonic at a given radius $r$ can be expressed as

$$K_{m,n}(r) = \frac{|E_{z_{m,n}}(r)|^2}{2\beta_n^2 P_z} \tag{6}$$

[see (1)] where $E_{z_{m,n}}$ and $\beta_n$ are calculated using (4) and (5), respectively.

The lowest order, fundamental FW mode for a helix SWS has mode numbers, $m = 0$, $n = 0$. The most important BW mode for a helix has $m = \pm 1$ and $n = 0$, where the $+$ corresponds to the BW mode on a clockwise-wound helix and the $-$ to the same mode on a counterclockwise helix. Note that since $E_{z_{m,n}}(r, \theta, z) \propto e^{jm\theta}$ and since the sign of the $m$-value depends on the handedness of the helix winding, we can think of the BW mode rotating with the helix as it propagates along its length.

### *B. Calculation of Off-Axis Interaction Impedance for Any Spatial Harmonic in a Ring-Bar Slow-Wave Structure*

The contrawound helix SWS [1] is composed of two oppositely wound helices with the same radii that are merged together, as shown in Fig. 1. The ring-bar SWS [2], shown in Fig. 2, is an approximate form of the contrawound helix in that it maintains the same symmetry and thereby behaves

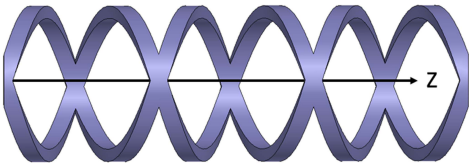


Fig. 1. Illustration of the contrawound SWS. The contrawound SWS is constructed by superimposing clockwise- and counterclockwise-wound monofilar helices.

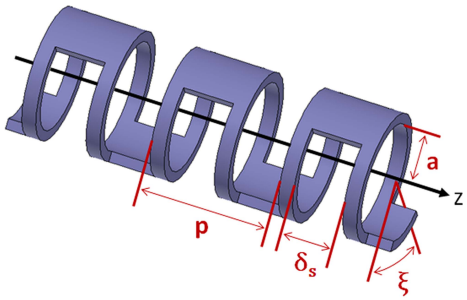


Fig. 2. Illustration of the ring-bar SWS. The ring-bar SWS has the same symmetric nature as the contrawound helix (the bars that connect the rings in the ring-bar SWS correspond to the crossing of the two helices in the contrawound SWS). The period, $p$, denotes the axial length of a single period of the SWS, $a$ is the inner radius, $\xi$ is the angular bar width, and $\delta_s$ denotes the axial distance between subsequent rings.

similarly electromagnetically. Since both the contrawound and ring-bar SWSs have oppositely oriented windings, using the equations for a monofilar helix as discussed above to calculate the interaction impedance for the BW mode results in two degenerate solutions: $m = +1$ and $m = -1$. Since both these solutions represent axially directed electric fields (with the same phase and group velocities) that can simultaneously couple with the electron beam, it is of interest to reformulate the equations above such that a single, nonzero solution is produced for both the fundamental FW and BW spatial harmonics in the contrawound/ring-bar SWS. We do this using a sine/cosine basis function set instead of the exponential during the expansion of the total electric field. This is consistent with the same choice made in [1] and [5].

The derivation of the appropriate solution starts by assuming that the total electric field takes the form

$$E_z(r, \theta, z) = \sum_{m=0}^{\infty} \sum_n \left[ E^C_{z_{m,n}}(r) \cos(m\theta) + E^S_{z_{m,n}}(r) \sin(m\theta) \right] e^{-j\beta_n z} \tag{7}$$

where $E^C_{z_{m,n}}(r)$ is the Fourier coefficient associated with the cosine term and $E^S_{z_{m,n}}(r)$ is associated with the sine term. Solving for the Fourier coefficients in a similar manner as

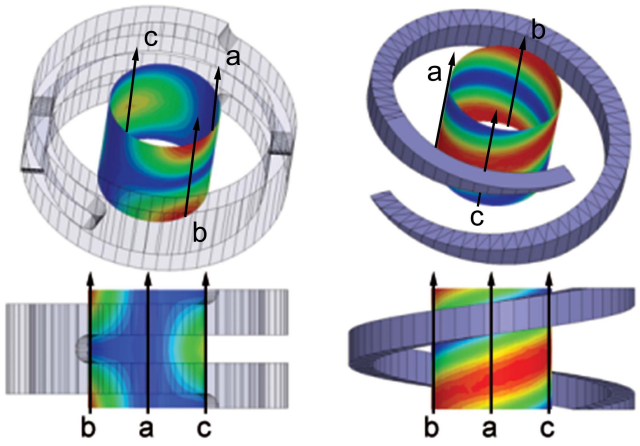


Fig. 3. HFSS calculated magnitude of the integrand in (4) and (8) for the BW in the ring bar (left) and helix (right), respectively. Colors: integrand magnitude, which is scaled from the highest shown in light red to the lowest shown in dark blue (each SWS is normalized to its own field strength). Images on the top and bottom represent different views of the same solution.

was done for the monofilar helix gives

$$E^{C}_{z_{m,n}}(r) = \begin{cases} \dfrac{1}{2\pi p}\displaystyle\int_0^p\int_0^{2\pi} E_z e^{j\beta_n z} d\theta dz, & m = 0 \\ \dfrac{1}{\pi p}\displaystyle\int_0^p\int_0^{2\pi} E_z \cos(m\theta) e^{j\beta_n z} d\theta dz, & m > 0 \end{cases} \quad (8)$$

$$E^{S}_{z_{m,n}}(r) = \begin{cases} 0, & m = 0 \\ \dfrac{1}{\pi p}\displaystyle\int_0^p\int_0^{2\pi} E_z \sin(m\theta) e^{j\beta_n z} d\theta dz, & m > 0 \end{cases} \quad (9)$$

where $E_z$ in (8) and (9) is defined over all space [(i.e., $E_z(r, \theta, z)$)]. A detailed summary of this derivation is provided in [15]. Finally, the values of $E^{C}_{z_{m,n}}$ and $E^{S}_{z_{m,n}}$ can be used to calculate the Pierce interaction impedance for a single space harmonic at a given radius, $r$, according to (6).

Having established the appropriate functional form for the axial electric field calculation, we next look at the 3-D electric field distributions of the BW mode. We plot the magnitude of the integrand (i.e., the magnitude of the axial electric field of the BW mode) of (8) with $m = 1$ and $n = 0$ for the ring-bar SWS and compare it to the magnitude of the integrand of (4) with $m = 1$ and $n = 0$ for a clockwise-wound monofilar helix, which corresponds to the BW mode in each respective SWS. These results were calculated at a radius equal to one-half the inner radius of the SWS and are shown in Fig. 3.

There is an important observation that can be made from Fig. 3. In the case of the monofilar helix, electrons traveling along cord a, b, or c (as shown in Fig. 3) will be subject to approximately the same axial electric field when averaged along the cord over the helix's pitch. However, for the ring bar, electrons traveling along cord a will be subject to significantly lower average axial electric fields when compared with electrons traveling along either cords b or c. This represents a significant difference in the fields of an idealized helix (monofilar or contrawound) and a realistic ring-bar structure. It may significantly explain why, the ring-bar SWS has been historically viewed as having a reduced BW interaction impedance. We will return to this point shortly. In any case, to be complete, we must calculate and examine the BW interaction impedance using the combined pitch and azimuthal averaged axial electric field (i.e., integration over both $z$ and $\theta$) as given in (8), which is done in Section III.

Before proceeding, however, we note the significance of this observation; namely that there exist azimuthal regions, which correspond to significantly reduced axial-directed electric fields for the BW mode in the ring bar. This could be used, for example, by a TWT designed with ring-bar SWS in conjunction with a sheet electron beam [16]. If the sheet beam's long axis was aligned with this reduced electric field region, one would see significant reduction in BW mode coupling. This concept could be extended by elongating the cross section of the ring-bar SWS into an oval or rectangular-shape allowing for a larger sheet beam to propagate.

## III. Comparison of Fundamental Forward-Wave and Backward-Wave Mode Interaction Impedance

Having established the method of calculating the interaction impedance for the ring-bar SWS, we next explore the magnitude of the BW interaction impedance. In particular, we do so by comparing its magnitude to the magnitude of the fundamental FW mode impedance. This comparison was explored previously [5], but used a different metric of comparison than we chose for this paper. The details of the previous, as well as the present, analysis are discussed in this section.

In [5], the axial electric field for the spatial harmonics in the ring-bar SWS was derived similarly to that discussed in [1], in which the total axial electric and magnetic fields were expanded in a Fourier series and solved to satisfy both the cylindrical wave equation and the boundary conditions inherent to the helical tape model [13]. Their solution took the form

$$E_z(r, \theta, z)_{r \le a} \propto \sum_{m=0}^{\infty}\sum_{n=-\infty}^{\infty} A_{m,n} \frac{I_m(\gamma_n r)}{I_m(\gamma_n a)} e^{-j\beta_n z} \cos(m\theta) \quad (10)$$

where $r$ is the electron beam radius, $a$ is the inner radius of the SWS, $m$ and $n$ are the harmonic mode numbers for which 0, 0 is the fundamental FW mode,[1] $A$ is the Fourier coefficient of the mode, $I_\chi$ is the modified Bessel function of the first kind with order $\chi$, and $\gamma_n^2 = \beta_n^2 - \omega^2/c^2$ where $\beta_n = \beta_0 + 2\pi n/p$, $\omega = 2\pi f$ where $f$ is the frequency, $c$ is the speed of light, $\beta_0$ is the fundamental FW mode wavenumber, and $p$ is the physical pitch of the SWS. It is important for later discussion to note from (10) that the radial variation of $E_z$ is described by $I_m$, which is finite for $r = 0$ when $m = 0$ (i.e., the fundamental FW mode) but goes to zero for $r = 0$ when $m > 0$ (i.e., the higher order azimuthal harmonics). In addition, note that for analytic tractability, the assumption was made in [5], to approximate the actual ring-bar SWS fields with the summed clockwise and counterclockwise idealized helical tape model [13] solutions. This can contribute to an

[1] Chodorow and Chu [1] and Ayers and Kirstein [5] define their mode numbering scheme using $l$ as the azimuthal mode number and $n$ as the axial mode number.

underestimate of the azimuthally averaged axial electric fields by neglecting the impact of high-field regions of actual ring-bar structures, such as those along cords b and c in Fig. 3. It is beyond the scope of this paper to determine comprehensive, general guidelines for the extent of error resulting from this idealized model assumption, but it can be expected to depend on the bar-length-to-pitch ratio.

The interaction impedances for the spatial harmonics were calculated in [5] from this solution. Given in [5, eq. (2.31)], the ratio between the higher order mode impedance and the fundamental FW mode impedance is given as

$$\left.\frac{K_{m,n}}{K_{0,0}}\right|_{r\le a} \approx F_1 F_2 \frac{I_m^2(\gamma_n r)}{I_m^2(\gamma_n a)} \frac{I_0^2(\gamma_0 a)}{I_0^2(\gamma_0 r)} \tag{11}$$

where $K_{m,n}$ is the interaction impedance of the $m, n$ mode and $F_1$ and $F_2$ are geometric factors that depend entirely on the geometry of the SWS given as

$$F_1(n, \alpha, \eta') = \left[\frac{\sin([n+\alpha]\eta'/2)}{(1+n/\alpha)^2 \sin(\alpha\eta'/2)}\right]^2 \tag{12}$$

$$F_2(m, \xi) = (2-\delta_m)\left[\frac{\cos(m\xi/2)}{1-m^2/d^2}\right]^2 \tag{13}$$

where $\alpha = \beta_0 a/\cot\psi$, $\psi$ is the SWS pitch angle given by $\cot\psi = 2\pi a/p$, $\eta' = 2\pi\delta_s/p$ where $\delta_s$ is the axial spacing between subsequent rings, and $\xi$ is the angular bar width, as shown in Fig. 2, $\delta_m$, the Kronecker delta, is given by

$$\delta_m = \begin{cases} 0, & m \neq 0 \\ 1, & m = 0 \end{cases} \tag{14}$$

and $d = \pi/(2\pi - \xi)$.

From (11), which is essentially a ratio of the respective electric axial fields defined in (10), we can make a very important observation about how this interaction impedance comparison is made. Namely, it is noted that the arguments of the Bessel functions for the higher order modes and the fundamental FW mode are both dependent on $\gamma_n$; all of which use the same $\omega$. In other words, using this formula, we are comparing the impedances of the higher order modes to the fundamental FW mode at the same frequency. This, however, is not the comparison we are interested in for this paper, nor is it the most appropriate when designing a TWT. Instead of comparing the impedances at a given frequency, we ought to compare the impedances at a given phase velocity. In particular, it is more appropriate to make this comparison at the phase velocity that corresponds to the electron beam's velocity.

To contrast the difference between a comparison using a common beam velocity versus a comparison using a common frequency, we first had to select a specific, nominal beam velocity and corresponding ring-bar SWS. For the beam velocity, we chose to examine a circuit intended to interact with a ~14-kV electron beam, consistent with the 12–15-kV electron beams typically cited in recent mmw TWT research [17]–[19]. To make our analysis similar to that presented in [5], we also chose to slightly idealize the circuit by considering only the ring-bar SWS, neglecting additional components, such as discrete dielectric rods or conducting barrel backwalls. Because of current interest in advanced high-power mmw amplifiers, we scaled the ring-bar dimensions to realize a fundamental FW interaction in the $Q$-band of frequencies, near 45 GHz. Using this electron beam and SWS, we used HFSS to calculate the dispersion characteristics. These results are plotted in Fig. 4 along with annotations that highlight the difference between comparing the BW and FW impedances at common frequency versus common beam velocity.

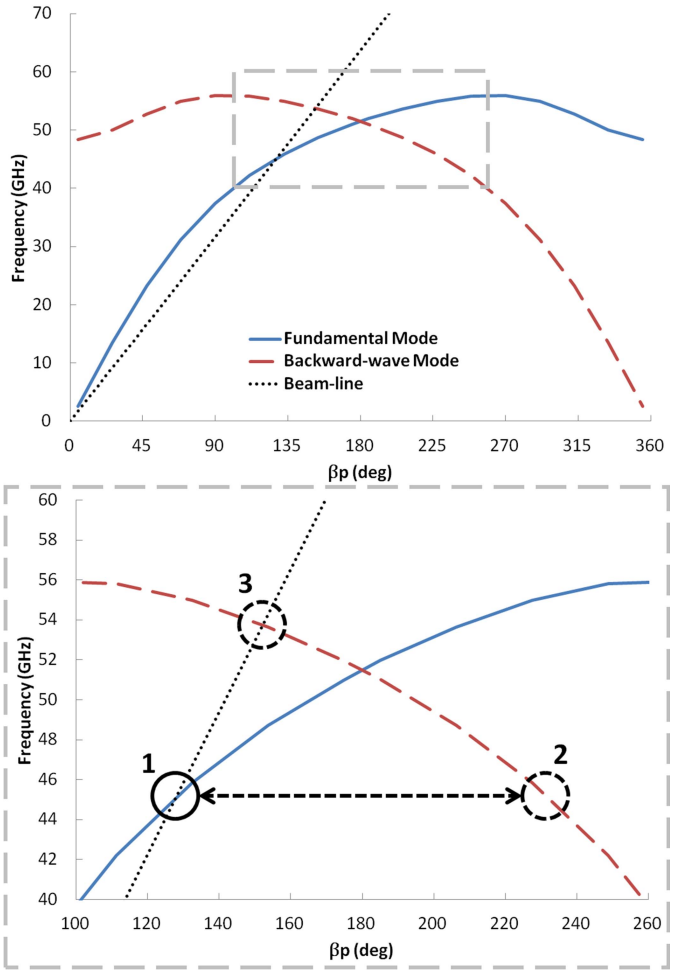


Fig. 4. Top: illustrative dispersion diagram for ring-bar SWS including beam line. Bottom: zoomed-in view of dispersion diagram near the interaction region. The interaction impedance comparison given in (11) is taken at a fixed frequency, which is equivalent to comparing the BW interaction impedance at circle 2 to the fundamental FW mode impedance at circle 1. For the purpose of this paper, however, we are interested in comparing the impedances at a constant phase velocity (i.e., at circles 1 and 3) as they correspond to the locations where the electron beam simultaneously interacts with the respective modes.

Using the same 14-kV electron beam and ring-bar SWS used to produce Fig. 4, we used HFSS and (6), (8), and (9) to calculate the ratio of the BW and the fundamental FW interaction impedance at a common beam velocity and a common frequency for different beam radii (normalized to the circuit radius $a$). We also used (11) to estimate the idealized ratio based on the simplified model of [5]. The results are shown in Fig. 5. The frequency corresponded to the frequency at which the beam line crossed the fundamental FW mode (near 45 GHz in this case) and the phase velocity corresponded to the 14-kV electron beam velocity.

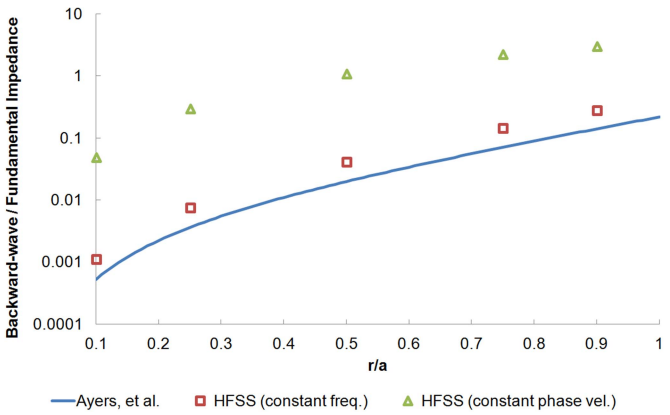


Fig. 5. Comparison of the HFSS calculated ratio of BW to fundamental FW mode interaction impedance at constant frequency and constant phase velocity and their comparison with the ratio calculated from (11) for the same SWS geometry.

As seen in Fig. 5, the analytic model underestimates the ratio, but is generally similar (same order of magnitude) to the more exact ratio calculated using HFSS for a common frequency. This verifies that (11) was formulated to compare the two impedances at a fixed frequency and not at a fixed beam (or phase) velocity.

For this specific example, we observe in Fig. 5 that the ratio of the impedances at a fixed velocity is approximately two orders of magnitude larger at small radii and approximately 1.5 orders of magnitude larger at larger radii than when we calculate the ratio at a fixed frequency. We find that for a specific example that the BW interaction impedance becomes larger than the fundamental FW mode impedance for $r \geq a/2$ when the comparison is completed at the electron beam velocity. This result is significant since the work completed in [1] and [5] is the basis for many of the subsequent publications and discussions regarding both the contrawound and ring-bar SWSs [2], [6], [7], [9], [10], [20]. The general conclusion from these previous publications is that the contrawound/ring-bar SWSs have vastly decreased BW interaction impedance. This present analysis, however, shows that there is at least one example of a ring-bar design for which this is not the case. Although this paper does not disprove any of the original results and is limited only to this specific example, it shows that care must be taken in generalizing the statement that the contrawound/ring-bar SWS has a decreased BW interaction impedance.

Unfortunately, comparing the BW and fundamental FW mode impedances between the ring-bar SWS and the helix SWS for a given set of operating parameters is problematic in that there is no single way to make the comparison. This is because the two SWSs have very different dispersion curves. For example, they can be compared when the relative geometries are approximately the same (resulting in different RF phase velocities since the contrawound/ring-bar SWS has an intrinsically faster phase velocity compared with a similarly dimensioned helix) or they can be compared when the two SWSs are designed to have the same phase velocity or interaction impedance at a given frequency (both of which result in comparing SWSs with very different dimensions). There are numerous free parameters in the design of these SWSs, making a direct side-by-side comparison difficult. A comprehensive comparison of the BW and fundamental FW mode interaction impedances between the ring-bar and helix SWS is left for a future research effort.

TABLE I
DESIGN GOALS FOR THE PROTOTYPE 45-GHz RING-BAR SWS

| | |
|---|---|
| Beam Voltage $(V)$ | 14400 |
| Beam current $(A)$ | 0.2 |
| Gain per stage $(dB)$ | ~20-30 |
| Saturated output power $(W)$ | 260 |
| Center Frequency | 45 GHz |

## IV. MILLIMETER-WAVE RING-BAR SWS DESIGN

Although the previous analysis suggests that ring-bar SWSs may not always suppress BW oscillation, they are still of interest. If designed correctly, they can still provide a higher fundamental interaction impedance and decreased BW impedance all in a larger radius package. These properties make them advantageous for high-power and high-frequency applications. In the remaining sections of this paper, we discuss the design of a mmw ring-bar SWS that was developed to illustrate this point.

The design dimensions and specifications for the ring-bar SWS were selected to be relevant for use in a mmw TWT. We chose to use similar parameters to the idealized $Q$-band SWS analyzed in Section III. We started with a nominal beam voltage of ~14 kV, and included typical circuit components, including dielectric rods and a conducting backwall. Slight adjustments were made to several parameters and dimensions until achieving a design with an intersection of the beam-velocity-line and the fundamental FW mode dispersion curve at ~45 GHz. The final beam voltage choice was 14.4 kV.

To evaluate the performance prospects for this circuit, we made additional assumptions about the beam, consistent with a set of nominal design goals listed in Table I.

Next, we analyzed the circuit with HFSS. The resulting FW and BW dispersion curves are shown in Fig. 6 along with the corresponding beam velocity line and the slow space charge wave velocity line.

Fig. 7 shows the comparison of the FW and BW interaction impedances between 35 and 55 GHz, calculated at the beam radius, taken to be half the circuit internal radius (corresponding to a 50% fill factor). To assist the comparison, the impedance values have been normalized to the value of the FW impedance at 35 GHz. The two boxes superimposed in Fig. 7 show that the ratio of the BW impedance at ~53.5 GHz (where the slow-space-charge wave velocity line and the BW dispersion curve intersect) to the FW impedance at ~45 GHz (where the beam and dispersion curves intersect) is ~0.79/0.95 = 0.83. Although this ratio is not much <1, recall from Fig. 5 that the impedance ratio taken at the beam radius overestimates the relative strength of the BW interaction, since the ratio is significantly smaller near the center of the beam. For that one pair of interactions,

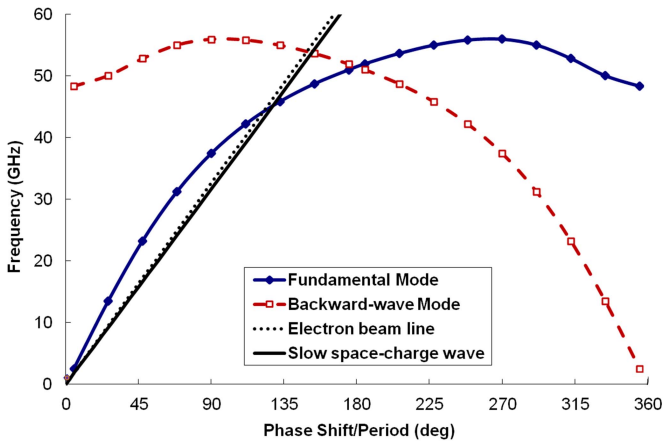


Fig. 6. Dispersion diagram for the prototype 45-GHz ring-bar SWS. The slow space-charge wave crosses the fundamental FW circuit mode at ~45 GHz and crosses the BW mode at ~53.7 GHz.

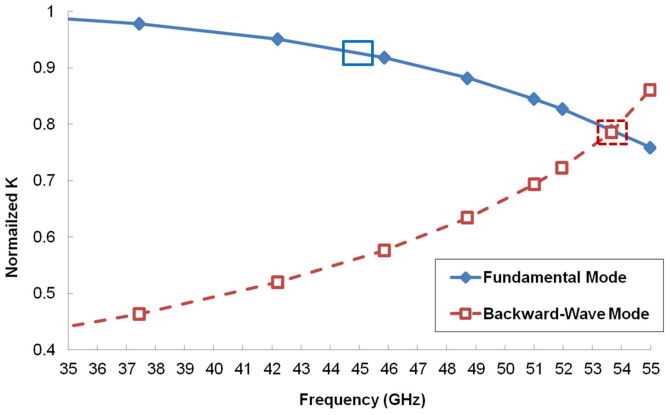


Fig. 7. Normalized FW and BW interaction impedance for the prototype 45-GHz ring-bar SWS. The superimposed boxes show where the slow space-charge wave of the 14.4-kV electron beam crosses the FW and BW modes, respectively.

the full beam averaged impedance ratio is approximately $\langle K_{\rm BW}/K_{\rm FW}\rangle = 0.23$. Although this is nonzero, it is still, in this case, significantly $<1$.

On a similar note, in Fig. 7, the FW and BW mode impedances are observed to cross at ~53.5 GHz, which is approximately the same frequency where the BW interacts with the electron beam (i.e., where the slow-space-charge wave velocity line crosses the BW dispersion curve). This is merely coincidental. Again, calculating the interaction impedance at the beam radius overestimates the BW impedance. Had we calculated the full beam averaged impedance, the FW and BW impedances would have crossed at a higher frequency while the BW and beam interaction would have remained at ~53.5 GHz.

To prepare for large-signal performance analysis as well as to enable comparisons with typical mmw TWT characteristics, we calculated the dimensionless Pierce gain parameter, $C$, the Pierce space-charge parameter, $4QC$, and the Pierce velocity parameter, $b$, which are defined as $C^3 \equiv I_0K/(4V_0)$, $4QC \equiv [\beta_q/(C\beta_e)]^2 = R_{sc}^2(\omega_p^2/\omega^2)/C^2$, and $b \equiv (\beta_p - \beta_e)/(\beta_e C) = (u_0 - v_p)/(v_p C)$, respectively. In these definitions, $I_0$ and $V_0$ are the dc electron beam current and accelerating voltage,

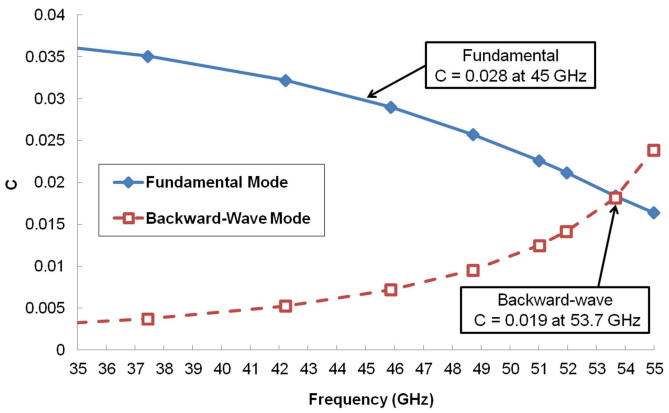


Fig. 8. Calculated Pierce gain parameter, $C$, of the prototype 45-GHz ring-bar SWS versus frequency. The slow space-charge wave of the 14.4-kV electron beam crosses the fundamental FW mode at 45 GHz, which corresponds to a $C$ value of 0.028 and crosses the BW mode at 53.7 GHz, which corresponds to $C = 0.019$.

respectively, and the Pierce interaction impedance, $K$, was discussed previously.

In the above expressions, the parameter, $\beta_p \equiv \omega/v_p$, is the axial wavenumber of the RF field as it propagates on the SWS without the beam present (commonly referred to as the cold circuit wavenumber) where $\omega$ is the operational frequency of the TWT and $v_p$ is the cold circuit phase velocity. The parameter $\beta_e \equiv \omega/u_0$ is the electron beam wavenumber where $u_0$ is the dc velocity of the electron beam. The parameter $\beta_q \equiv \omega_q/u_0$ is the reduced space-charge wavenumber where $\omega_q \equiv R_{\rm sc}\omega_p$, $R_{\rm sc}$ is the plasma frequency reduction factor [21]–[23], in which the beam's plasma frequency is given by $\omega_p^2 \equiv e\rho/(m\epsilon_0)$, $\rho$ is the volume charge density of the beam, $e$ and $m$ are the charge and mass of an electron, respectively, and $\epsilon_o$ is the permittivity of free space.

The results are presented in Figs. 8–10, were we also specify the values where the slow space-charge wave of the beam intersects the circuit dispersion curve as this is the general location where the interaction between the RF wave and electron beam occurs in a TWT. In general, these results are consistent with values typical for modern mmw high-power TWTs [11], [23]–[25].

Large-signal simulations were completed for the theoretical TWT using the designed SWS and specified electron beam, and the results are shown in Fig. 11. A maximum saturated output power of 260 W, corresponding to a gain of 54.2 dB, was predicted for a two-stage, 4.1-in long interaction length. An instantaneous 3-dB bandwidth of ~3% was predicted with a center frequency of 45 GHz.

## V. Experimental Methods and Results

All of the previous results were obtained from computational predictions using HFSS. To get an estimate for the accuracy of these predictions, we had several copies of this design study circuit fabricated for experimental measurements of their EM properties. To prepare for the measurements, we designed a cold test assembly (CTA). In a typical TWT, the SWS is housed in a vacuum envelope that becomes sealed once

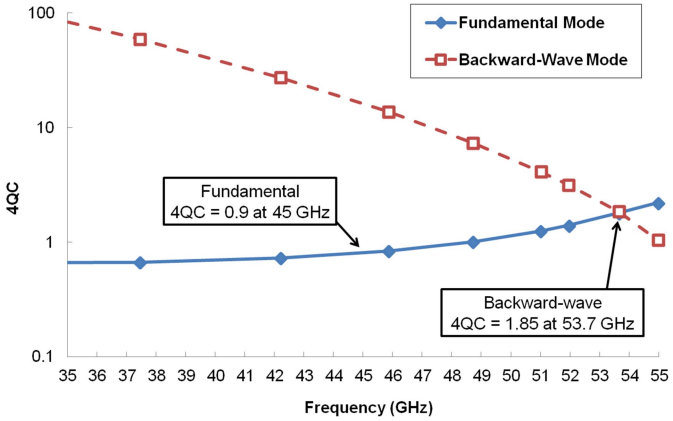


Fig. 9. Calculated Pierce space-charge parameter, $4QC$, of the prototype 45-GHz ring-bar SWS versus frequency. The slow space-charge wave of the 14.4-kV electron beam crosses the fundamental FW mode at 45 GHz, which corresponds to a $4QC$ value of 0.9 and crosses the BW mode at 53.7 GHz, which corresponds to $4QC = 1.85$.

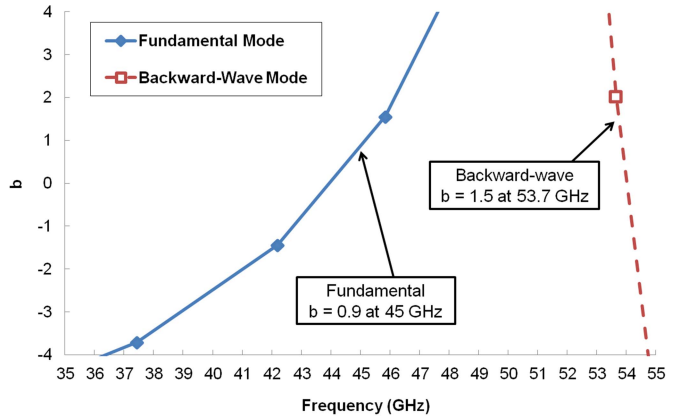


Fig. 10. Calculated Pierce velocity parameter, $b$, of the prototype 45-GHz ring-bar SWS versus frequency. The slow space-charge wave of the 14.4-kV electron beam crosses the fundamental FW mode at 45 GHz, which corresponds to a $b$ value of 0.9 and crosses the BW mode at 53.7 GHz, which corresponds to $b = 1.5$.

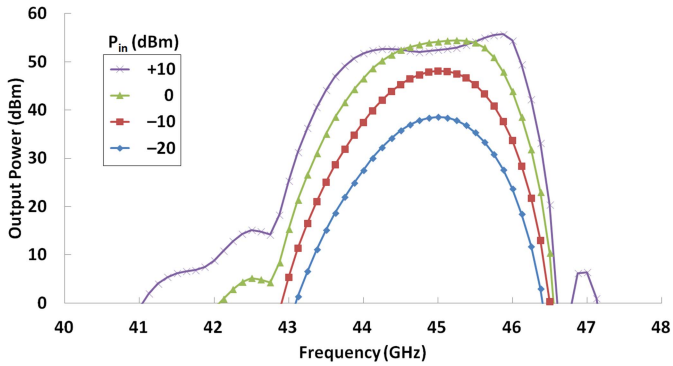


Fig. 11. Constant drive curves predicted by CHRISTINE-1-D for the two-stage, 14.4-kV, 45-GHz ring-bar TWT design. A maximum gain of ~54 dB is predicted with a ~3% 3-dB instantaneous bandwidth.

the SWS is packaged. For this body of work, however, it was of interest to produce a CTA that would allow the SWS to be interchanged. This was possible since we were only interested in cold-test measurements (i.e., without the electron beam present, thereby eliminating the need for operation/testing under vacuum). A clam-shell CTA was designed and built allowing for the SWS under test to be interchanged.

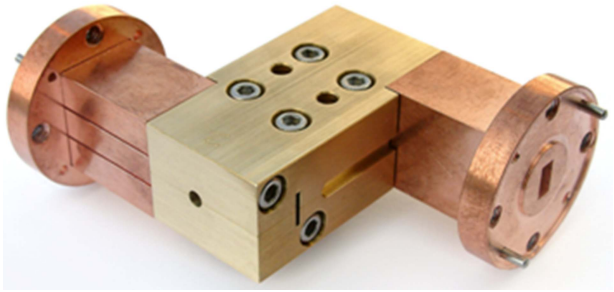

Fig. 12. Assembled CTA. Coupling to and from the CTA is accomplished via WR-22 waveguides attached to the CTA shown at the left and right sides of the image, each terminated with a WR-22 anticocking flange.

Both the SWS and CTA were custom fabricated by L-3 Communications-Electron Devices Division in San Carlos, CA.

The HFSS computations yielded predictions of the phase velocity and interaction impedance characteristics of these circuits. For validation, direct measurements of the phase velocity are straightforward, but measurements of the interaction impedance are very difficult and much less reliable. Therefore, we elected to test the accuracy of the modeling by conducting direct comparisons of experimental measurements and HFSS predictions of phase velocity and S-parameters for the circuits mounted in the CTA. Consistency between measurements and predictions for these parameters was considered sufficient to assume that the model's impedance predictions were also accurate.

The body of the CTA is shown in Fig. 12 and was fabricated from a ~2 × 1 × 0.5 block of gold-plated copper that was split in half on the 0.5 dimension. The cylindrical backwall for the SWS was fabricated by machining half a cylindrical groove into each half of the CTA along its long dimension. When the CTA was assembled, the cylindrical grooves combined to form a hollow cylinder down the center of the CTA along which the SWS was positioned. The SWS was held in the radial center of this cylinder using beryllium oxide (BeO) rods. The halves of the CTA were aligned during assembly using precision-ground pins and the entire assembly was held together by compression via screws. E-plane probe antennas similar to those used in [26] were used on each end of the SWS to couple to copper WR-22 waveguides on the respective end of the CTA.

The S-parameters of the entire cold-test experiment were predicted using the HFSS driven modal solution solver. A full-scale model of the entire experiment was drawn and simulated, including the full-length SWS housed within the assembled CTA (including both the clam-shell halves and the waveguide couplers). This simulation predicted the S-parameters, as they would be measured from the actual waveguide ports on the CTA.

A full set of S-parameters were measured for each of the nine SWSs constructed using an Agilent 8364 per-

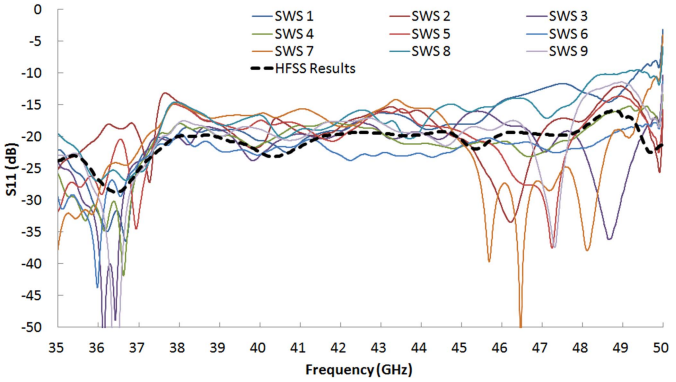


Fig. 13. Measured $S_{11}$ for each of the nine fabricated ring-bar SWSs compared with $S_{11}$ predicted by the HFSS model.

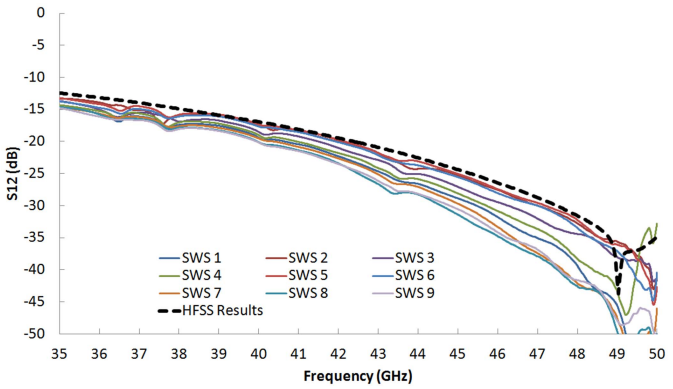


Fig. 14. Measured $S_{12}$ for each of the nine fabricated ring-bar SWSs compared with $S_{12}$ predicted by the HFSS model.

formance network analyzer. A different set of rods were used for each SWS, but the orientation of the rods with respect to each SWS was approximately the same due to the use of a precision alignment fixture. The S-parameters were measured from 25 to 50 GHz and the effect of the waveguide-to-CTA transition was gated out of the $S11$ and $S22$ results.

The phase velocity of each SWS was calculated as

$$v_{ph} = \frac{\Delta\theta}{\Delta z} \tag{15}$$

where the change in phase advance, $\Delta\theta$, was measured as a function of change in position along the axial length of the SWS, $\Delta z$. For this measurement a small-diameter coaxial probe, positioned within the ID of the SWS, was used as a positional RF exciter [27]. The OD of the probe was $\sim$80% the ID of the SWS; this ensured that the tip of the probe was approximately centered radially within the SWS. The probe's tip length (i.e., the axial length of exposed inner conductor) was set to $\sim$15% of the wavelength of a 45-GHz signal propagating on the SWS. This probe length was found to reliably and repeatably measure the change in phase as the probe was moved down the axis of the SWS. The position of the probe within the SWS was controlled using an automated, precision linear translation stage capable of controlling position-to-position movements to $\pm$0.00005 in (1.27 $\mu$m).

### A. S-Parameter Data

The results of the S-parameter measurements for the nine fabricated SWSs are presented in Figs. 13–15. Each S-parameter is compared with the corresponding HFSS prediction.

### B. Phase Velocity Data

The phase velocity of each of the nine fabricated SWSs was measured and calculated as described above and the results are presented in Fig. 16. The measured results are compared with the predicted phase velocity from the HFSS model.

## VI. Discussion

In general, the HFSS model predicted the behavior of the experimentally measured reflection parameters ($S_{11}$ and $S_{22}$)

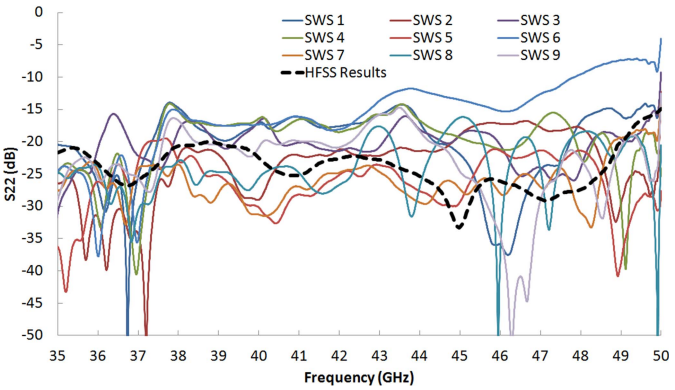


Fig. 15. Measured $S_{22}$ for each of the nine fabricated ring-bar SWSs compared with $S_{22}$ predicted by the HFSS model.

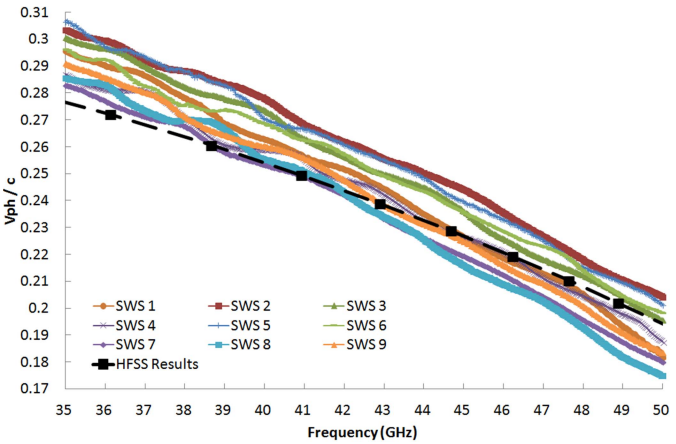


Fig. 16. Measured phase velocity of each of the nine fabricated ring-bar SWSs compared with the phase velocity predicted by the HFSS model.

for the ensemble of SWSs that were built and tested. A transmission of better than 90% was achieved (i.e., less than $-10$ dB $S_{11}$ and $S_{22}$) for each of the SWSs over most of the experimental bandwidth of interest (i.e., 40–48 GHz). Note that the WR22 waveguide used on the CTA is designed to operate between 33 and 50 GHz.

In addition to consistent reflection data, we found relatively good agreement between the experimental and modeled $S_{12}$ data. In general, the $S_{12}$ of the experimental measurements was slightly lower than the HFSS prediction. Although we did

specify material-specific RF losses in the HFSS model, it is likely that those losses were greater in the actual experiment. Material-specific losses within the mmw regime are not always well characterized and, even when they are, they depend heavily on parameters, such as surface roughness. Overall, even though the absolute values of the experimental $S_{12}$ data were slightly lower than predicted by HFSS, the HFSS model did predict the overall qualitative trend very well.

In Fig. 16, it is observed that the average phase velocity is distinctly different than the HFSS predicted phase velocity particularly at the lower end of the test band. In general, the measured phase velocity is more dispersive than was predicted by HFSS and varies significantly from SWS to SWS (up to $\sim$10%). Again, material specific parameters, such as the dielectric constant of the BeO rods and/or the conductivity of the SWS and CTA may have played a role in these differences. Best guess estimates for these parameters were used in the HFSS model but it is possible that not only did these parameters differ in absolute value for any given SWS, but that they also differed by a significant amount from SWS to SWS. In addition to these material specific parameters, fabrication or assembly discrepancies (such as the amount of compression applied to the CTA halves during assembly) may have also impacted the phase velocity of each SWS. Precision dimensional measurements of the ensemble of fabricated SWSs demonstrated that critical dimensions, including pitch, arc length of the bar (connecting adjacent rings), SWS ID, backwall ID, and rod width varied by up to 2.4%, 1.8%, 2.1%, 2.0%, and 7.5%, respectively. These variations occurred not only from SWS to SWS, but also along the length of each individual SWS. Subsequent modeling found that each of these types/magnitudes of errors could independently change the phase velocity by up to 3.8%. Although we did not model all of these dimensional errors simultaneously in a single simulation it is likely that, cumulatively, these critical dimensional variations were a primary cause of the $\sim$10% phase velocity differences observed in Fig. 16. In spite of the differences between model predictions and measurements of phase velocity and S-parameters, the results were in sufficient agreement to support the general conclusions reached in the previous portions of this paper, based upon the HFSS calculations of interaction impedance and general TWT parameters and performance.

## VII. Conclusion

In this paper, we derived and discussed the appropriate way to calculate the BW interaction impedance for a contrawound/ring-bar SWS. In particular, a sine and cosine basis function set are used during the expansion of the axial electric field since the electric field for this type of SWS may be thought of as a superposition of the fields of two separate helices (i.e., the clockwise and counterclockwise windings in the contrawound SWS). Using this solution, we examined the BW mode in the ring-bar SWS and found azimuthal locations that corresponded to significantly reduce axial electric fields. In addition, we calculated the ratio of the BW and fundamental FW mode interaction impedances for the ring-bar SWS and compared it to the previously published analytic calculation. We found that comparing these impedances at a given phase velocity (as opposed to a given frequency) results in a significantly larger BW impedance than the previous calculation suggests. In general, this paper shows that the BW interaction impedance is not always significantly suppressed in the contrawound/ring-bar SWS. However, the BW mode is still moderately suppressed for fill factors <50%.

After summarizing the difficulties inherent in general comparisons of ring-bar or contrawound SWS TWTs and monofilar helix TWTs, we examined an illustrative mmw ring-bar SWS designed and fabricated for a 45-GHz, 14.4-kV, 260-W TWT. In addition, a clam-shell CTA was designed to facilitate the measurement of the S-parameters and phase velocity of the SWS. The clam-shell design allowed multiple SWSs to be tested with a single test assembly. The S-parameters and phase velocity of nine prototype SWSs were measured and presented. Good consistency between the measurements and the HFSS simulations was observed although the measured SWSs appeared to be slightly more dispersive than the simulation predicted. The results confirmed that ring-bar SWSs remain attractive for high-power mmw TWTs. They offer an opportunity for high power and high gain with reduced BW oscillation susceptibility. However, this paper illustrates that BW suppression cannot be assumed a guaranteed universal feature of contrawound or ring-bar SWSs. Therefore, each design should be independently examined for BW oscillation vulnerability.

## Acknowledgment

The authors would like to thank both C. Marotta and M. Martin (both from L-3 EDD) for their invaluable assistance with the design and construction of the CTA as well as with the measurements of the ring-bar test circuits. They would also like to thank the former president of L-3 EDD, J. Benham, for his outstanding support of this paper.

## References

[1] M. Chodorow and E. L. Chu, "Cross-wound twin helices for traveling-wave tubes," *J. Appl. Phys.*, vol. 26, no. 1, pp. 33–43, Jan. 1955.

[2] C. K. Birdsall and T. E. Everhart, "Modified contra-wound helix circuits for high-power traveling-wave tubes," *IRE Trans. Electron Devices*, vol. 3, no. 4, pp. 190–204, Oct. 1956.

[3] O. Sauseng, "Ring-bar slow-wave structures for wideband high power TWTs in the millimeter wave range," in *IEDM Tech. Dig.*, 1982, p. 22.

[4] S. Liu, "Estimation of RF parameters for millimeter wave ring-bar TWTs," *Int. J. Infr. Millimeter Waves*, vol. 21, no. 5, pp. 745–750, 2000.

[5] W. R. Ayers and P. T. Kirstein, "Theoretical and experimental characteristics of connected-ring structures for use in high-power traveling-wave tubes," Microw. Lab., Stanford Univ., Stanford, CA, USA, Tech. Rep. 358, Jan. 1957.

[6] J. E. Nevins, Jr., "An investigation and application of the contrawound helix," *IRE Trans. Electron Devices*, vol. 6, no. 2, pp. 195–202, Apr. 1959.

[7] W. N. Cain and R. W. Grow, "The effects of dielectric and metal loading on the dispersion characteristics for contrawound helix circuits used in high-power traveling-wave tubes," *IEEE Trans. Electron Devices*, vol. 37, no. 6, pp. 1566–1578, Jun. 1990.

[8] (2014, Nov. 7). *Ansys HFSS*. [Online]. Available: http://www.ansys.com/Products/Simulation+Technology/Electronics/Signal+Integrity/ANSYS+HFSS

[9] D. T. Lopes and C. C. Motta, "Characterization of ring-bar and contrawound helix circuits for high-power traveling-wave tubes," *IEEE Trans. Electron Devices*, vol. 55, no. 9, pp. 2498–2504, Sep. 2008.

[10] A. S. Gilmour, *Principles of Traveling Wave Tubes*. Norwood, MA, USA: Artech House, 1994.
[11] J. H. Booske and M. C. Converse, "Insights from one-dimensional linearized Pierce theory about wideband traveling-wave tubes with high space charge," *IEEE Trans. Plasma Sci.*, vol. 32, no. 3, pp. 1066–1072, Jun. 2004.
[12] J. R. Pierce, *Traveling Wave Tubes*. Princeton, NJ, USA: Van Nostrand, 1950.
[13] S. Sensiper, "Electromagnetic wave propagation on helical structures," *Proc. IRE*, vol. 43, no. 2, pp. 149–161, Feb. 1955.
[14] S. J. Cooke *et al.*, "CTLSS—An advanced electromagnetic simulation tool for designing high-power microwave sources," *IEEE Trans. Plasma Sci.*, vol. 28, no. 3, pp. 841–866, Jun. 2000.
[15] S. Sengele, "Impact of random fabrication errors on the performance of a contrawound helix slow-wave structure for a millimeter-wave traveling wave tube," Ph.D. dissertation, Dept. Elect. Eng., Univ. Wisconsin-Madison, Madison, WI, USA, 2012.
[16] M. A. Basten, J. H. Booske, J. Anderson, and J. E. Scharer, "Formation and transport of sheet-electron beams and multibeam configurations for high-power microwave devices," *Proc. SPIE*, vol. 2557, p. 262, Jul. 1995.
[17] C. K. Chong *et al.*, "Development of high power Ka/Q dual-band and communications/radar dual-function helix-TWT," *IEEE Trans. Electron Devices*, vol. 56, no. 5, pp. 913–918, May 2009.
[18] A. Scott, "Millimeter wave power modules: Are they a marriage made in heaven?" in *Proc. Int. Vac. Electron. Conf.*, May 2000, p. 22.2.
[19] V. Srivastava, "THz vacuum microelectronic devices," in *Proc. Int. Symp. Vac. Sci. Technol.*, 2008, pp. 1–10.
[20] J. F. Gittins, *Power Traveling-Wave Tubes*. New York, NY, USA: American Elsevier, 1965.
[21] J. E. Rowe, *Nonlinear Electron-Wave Interaction Phenomenon*. New York, NY, USA: Academic, 1965.
[22] R. G. Hutter, *Beam and Wave Electronics in Microwave Tubes*. Princeton, NJ, USA: Van Nostrand, 1960.
[23] Y. Y. Lau and D. Chernin, "A review of the ac space-charge effect in electron–circuit interactions," *Phys. Fluids B*, vol. 4, no. 11, pp. 3473–3497, Nov. 1992.
[24] J. H. Booske, "Plasma physics and related challenges of millimeter-wave-to-terahertz and high power microwave generation," *Phys. Plasmas*, vol. 15, no. 5, pp. 055502-1–055502-16, Feb. 2008.
[25] P. Pengvanich, D. Chernin, Y. Y. Lau, J. W. Luginsland, and R. M. Gilgenbach, "Effect of random circuit fabrication errors on small-signal gain and phase in traveling-wave tubes," *IEEE Trans. Electron Devices*, vol. 55, no. 3, pp. 916–924, Mar. 2008.
[26] S. Sengele, H. Jiang, J. H. Booske, D. van der Weide, C. Kory, and L. Ives, "A selectively metallized, microfabricated W-band meander line TWT circuit," in *Proc. IEEE Int. Vac. Electron. Conf.*, Apr. 2008, pp. 18–19.
[27] J. R. Legarra, "Measurement of microwave characteristics of helix traveling wave circuits," in *Proc. Int. Electron Devices Meeting*, Washington, DC, USA, Dec. 1979, pp. 408–411.

**Sean Sengele** (S'06–M'12) received the B.S., M.S., and Ph.D. degrees in electrical engineering from the University of Wisconsin-Madison, Madison, WI, USA, in 2004, 2008, and 2012, respectively.

He had internships with the Electron Devices Division (EDD), L-3 Communications, San Carlos, CA, USA, in 2003, and with the Los Alamos National Laboratory, Los Alamos, NM, USA, in 2004. Both experiences gave him broad exposure to the area of vacuum electronics. From 2009 to 2011, he was with EDD, while completing his Ph.D. dissertation. Since 2012, he has been a Research Engineer with the Sensors and Electromagnetic Applications Laboratory, Georgia Tech Research Institute, Smyrna, GA, USA. His current research interests include millimeter-wave and terahertz system engineering, vacuum electronics, next-generation radar and electronic warfare systems, and RF microelectromechanical systems.

Dr. Sengele is currently the acting Treasurer of the Atlanta Joint Chapter of the IEEE Antennas and Propagation, and Microwave Theory and Techniques Societies.

**Marc L. Barsanti** was with the U.S. Naval Research Laboratory, Washington, DC, USA, Northrop Grumman, Falls Church, VA, USA, and Litton Industries, Milwaukee, WI, USA. He has been involved in the microwave tube industry since 1985. He is currently the Engineering Manager of Mini-Helix Traveling Wave Tubes with L-3 Communications, San Carlos, CA, USA.

**Thomas A. Hargreaves** (M'92) received the B.S. degree in mathematics, the M.S. degree in engineering applied science, and the Ph.D. degree in plasma physics from the University of California at Davis, Davis, CA, USA, in 1976, 1978, and 1982, respectively.

He was with Jaycor International, Sandton, South Africa, Mission Research Corporation, Santa Barbara, CA, USA, and the U.S. Naval Research Laboratory, Washington, DC, USA, from 1983 to 1991, where he worked on a variety of high-power microwave (HPM) and millimeter-wave projects, including source development and HPM effects testing. In 1991, he joined the Electron Devices Division (EDD) at L-3 Communications, San Carlos, CA, USA, as a Senior Scientist, where he was responsible for the design and development of microwave devices, including a 94-GHz harmonic gyroklystron, a 200-MW C-band klystron, and a 2.5-MW 805-MHz klystron. Since 2003, he has been involved in a wide range of helix traveling wave tubes for both the military and commercial markets.

Dr. Hargreaves is a member of the American Physical Society. He was a co-recipient of the Robert L. Woods Award for Excellence in Vacuum Electronics Technology in 1999.

**Carter M. Armstrong** (SM'08–F'13) received the bachelor's degree in physics from Rutgers University, New Brunswick, NJ, USA, and the Ph.D. degree in plasma physics from the University of Maryland, College Park, MD, USA.

He is currently the Vice President of Engineering with the Electron Devices Division, L-3 Communications, San Carlos, CA, USA. He is also an Adjunct Professor with the Department of Electrical and Computer Engineering, University of Wisconsin-Madison, Madison, WI, USA. He has authored the technology article entitled The Truth About Terahertz in the 2012 September issue of *IEEE Spectrum*.

Dr. Armstrong was a recipient of the 2013 IEEE John R. Pierce Award for Excellence in Vacuum Electronics in Paris, France.

**John H. Booske** (S'82–M'85–SM'93–F'07) received the Ph.D. degree in nuclear engineering from the University of Michigan, Ann Arbor, MI, USA, in 1985.

He was a Research Scientist with the University of Maryland, College Park, MD, USA, from 1985 to 1989, researching magnetically confined hot ion plasmas and sheet-electron-beam free electron lasers. Since 1990, he has been with the faculty of the Department of Electrical and Computer Engineering, University of Wisconsin-Madison (UW), Madison, WI, USA, where he is currently the Chair of the Department, the Director of the Wisconsin Collaboratory for Enhanced Learning (a learning space that supports IT-assisted peer-collaborative learning), and the Duane H. and Dorothy M. Bluemke Professor of Engineering. From 2001 to 2005, he served as the Director of the Interdisciplinary Materials Science Program at UW. He co-edited the books entitled *Microwave and Radio Frequency Applications* (American Ceramic Society, 2003) and *Microwave and Millimeter-Wave Power Electronics* (IEEE/Wiley, 2005). His research interests include experimental and theoretical study of coherent electromagnetic radiation, its sources and its applications, and spanning the RF, microwave, millimeter-wave, and terahertz (THz) regimes. His current research activities include vacuum electronics, microfabrication of millimeter-wave and THz regime sources and components, high-power microwaves, advanced cathodes, physics of the interaction of THz radiation and materials, microwave-generated plasma discharges, and biological applications of electric and electromagnetic fields.

Prof. Booske is a fellow of the American Physical Society in 2011. He has been a Guest Editor of the IEEE TRANSACTIONS ON PLASMA SCIENCE. He was a recipient of the UW Vilas Associate Award for research and the U.S. National Science Foundation Presidential Young Investigator Award. He has received many teaching awards, including the UW Chancellors Distinguished Teaching Award, the UW Teaching and Learning Innovation Award, and the IEEE EAB Major Educational Innovation Award.

**Yue-Ying Lau** (M'98–SM'06–F'08) received the B.S., M.S., and Ph.D. degrees in electrical engineering from the Massachusetts Institute of Technology, Cambridge, MA, USA.

He is currently a Professor with the University of Michigan, Ann Arbor, MI, USA, specialized in RF sources, heating, and discharge.

Prof. Lau is a fellow of Antennas and Propagation Society. He was a recipient of the IEEE Plasma Science and Applications Award.